Multiband Effects in the Superconducting Phase Diagram of Oxide Interfaces

Alexis Jouan, Simon Hurand, Gyanendra Singh, Edouard Lesne, Agnés Barthélémy, Manuel Bibes, Christian Ulysse, Guilhem Saiz, Chéryl Feuillet-Palma, Jérôme Lesueur, et al.

CHALMERS
UNIVERSITY OF TECHNOLOGY

Multiband Effects in the Superconducting Phase Diagram of Oxide Interfaces

ADVANCED MATERIALS INTERFACES
www.advmatinterfaces.de

Multiband Effects in the Superconducting Phase Diagram of Oxide Interfaces

*Alexis Jouan, Simon Hurand, Gyanendra Singh, Edouard Lesne, Agnés Barthélémy, Manuel Bibes, Christian Ulysse, Guilhem Saiz, Chéryl Feuillet-Palma, Jérôme Lesueur, and Nicolas Bergeal**

A dome-shaped phase diagram of superconducting critical temperature upon doping is often considered as a hallmark of unconventional superconductors. This behavior, observed in $SrTiO_3$-based interfaces, whose electronic density is controlled by field-effect, has not been explained unambiguously yet. Here, a generic scenario for the superconducting phase diagram of these oxide interfaces is elaborated based on transport experiments on a double-gate $LaAlO_3/SrTiO_3$ field-effect device and Schrödinger–Poisson numerical simulations of the quantum well. The optimal doping point of maximum T_c is ascribed to the transition between a single-gap and a fragile two-gap $s_{\pm}$-wave superconducting state involving bands of different orbital character. Close to this point, a bifurcation in the dependence of T_c on the carrier density, which can be controlled by the details of the doping execution, is observed experimentally and reproduced by numerical simulations. Where doping with a back-gate triggers the filling of a new d_{xy} subband and initiates the overdoped regime, doping with a top-gate delays the filling of the subband and maintains the 2D electron gaz in the single-gap state of higher T_c. Such a bifurcation, whose branches can be followed reversibly, provides a generic explanation for the dome-shaped superconducting phase diagram that could be extended to other multiband superconducting materials.

1. Introduction

The superconducting 2D electron gas (2-DEG) that forms at the interface between two insulating oxides, such as in $LaAlO_3/SrTiO_3$ and $LaTiO_3/SrTiO_3$ heterostructures, exhibits a complex phase diagram controlled by the electron density.[1,2] While the system is in a weakly insulating state at low density, superconductivity emerges when electrons are added by means of electrostatic gating resorting to a back-gate, a side-gate, or a top-gate geometry[1,3,4] (**Figure 1**). When the carrier density (n_{2D}) increases, the superconducting T_c rises to a maximum value, $T_c^{max} \approx 300$ mK, before decreasing as doping is further increased. The resulting dome-shaped superconducting phase diagram resembles that observed in other families of superconductors, including high-T_c cuprates, Fe-based superconductors, heavy fermions, and organic superconductors.[5,6] Two noticeable doping points are universally observed in the phase diagram of oxide interfaces: a quantum critical point (QCP) at low density that separates a weakly insulating region and a superconducting one, and a maximum critical temperature point (T_c^{max}) at an optimal doping that defines the frontier between the underdoped regime and the overdoped one. Despite much research efforts, there is not yet a consensus on the origin of these two points. In $LaAlO_3/SrTiO_3$ heterostructures, electrons

A. Jouan, G. Saiz, C. Feuillet-Palma, J. Lesueur, N. Bergeal
Laboratoire de Physique et d'Etude des Matériaux
ESPCI Paris
Université PSL
CNRS
Sorbonne Université
10 rue Vauquelin, Paris 75005, France
E-mail: nicolas.bergeal@espci.fr

S. Hurand
Institut Pprime
UPR 3346 CNRS
Université de Poitiers
ISAE-ENSMA, BP 30179, Futuroscope-Chasseneuil Cedex
86962, France

The ORCID identification number(s) for the author(s) of this article can be found under https://doi.org/10.1002/admi.202201392.

DOI: 10.1002/admi.202201392

G. Singh
Quantum Device Physics Laboratory
Department of Microtechnology and Nanoscience MC2
Chalmers University of Technology
Gothenburg SE-412 96, Sweden

E. Lesne
Max Planck Institute for Chemical Physics of Solids
01187 Dresden, Germany

A. Barthélémy, M. Bibes
Unité Mixte de Physique CNRS-Thales
Université Paris-Sud, Université Paris-Saclay
1 Av. A. Fresnel, Palaiseau 91767, France

C. Ulysse
Centre for Nanoscience and Nanotechnology
CNRS
Université Paris-Saclay
10 Bd Thomas Gobert, Palaiseau 91120, France

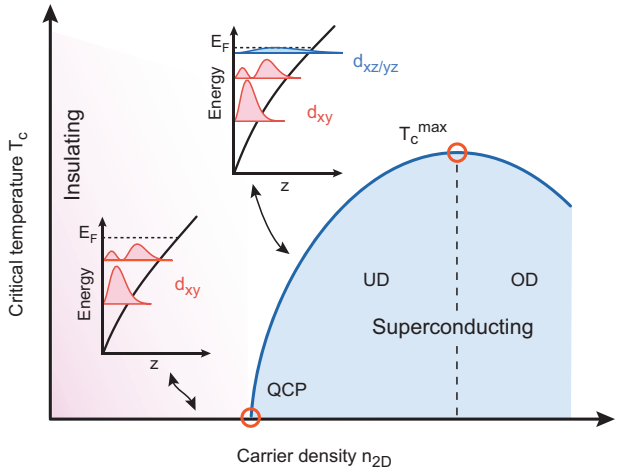

Figure 1. Schematic description of the dome-shaped superconducting phase diagram of (001)-oriented $LaAlO_3/SrTiO_3$ interfaces. The QCP marks the emergence of superconductivity at a critical carrier density corresponding the filling of the $d_{xz/yz}$ heavy bands depicted by the sketch of the interfacial band structure. An optimal doping point corresponding to T_c^{max} separates an underdoped (UD) region where T_c increases with n_{2D} and an overdoped (OD) region where T_c decreases with n_{2D}.

are trapped in an asymmetric quantum well that extends on the $SrTiO_3$ side and accommodates a set of discrete t_{2g}-based subbands (see insets in Figure 1).[7–10] The d_{xy} subbands are energetically the lowest lying orbitals with a pronounced 2D character. Sitting higher in energy in the quantum well, the degenerate $d_{xz/yz}$ subbands delocalize deeper in the $SrTiO_3$ substrate, where they recover bulk-like properties, including a high dielectric permittivity and reduced scattering. Several studies have pointed out the connection between superconductivity and the filling threshold of the degenerate $d_{xz/yz}$ subbands, whose high density of states favors the emergence of superconductivity.[11,12] However, the T_c^{max} point at the top of the dome, remains largely unexplained. Among a few different scenarios, it has been suggested that the suppression of T_c in the overdoped regime could result from a strong pair breaking scattering in the presence of opposite-sign gaps $s_{\pm}$-wave superconductivity.[13,14] In 1980, Binnig et al. reported a double-gap structure in tunneling spectroscopy experiments performed on Nb-doped bulk $SrTiO_3$ demonstrating that the different t_{2g} bands could accommodate several superconducting condensates.[15] More recently, signatures of two-gap superconductivity consistent with a $s_{\pm}$-wave state were clearly observed in (110)-oriented $LaAlO_3/SrTiO_4$ interfaces in superfluid stiffness and critical field measurements.[16,17] Josephson experiments suggest that such state could also take place in the conventional (001)-oriented $LaAlO_3/SrTiO_3$ interfaces.[18,19]

In this letter, we analyze the transport properties of a double-gate $LaAlO_3/SrTiO_3$ field-effect device. We evidence a bifurcation in the dependence of T_c on the carrier density n_{2D} when the 2-DEG is electrostatically doped either with a top-gate or a back-gate. To explain this behavior we used numerical simulations of the self-consistent Schrödinger–Poisson equations and show that different superconducting regimes related to different subband occupations can be accessed close to the optimal doping level. The suppression of T_c in the overdoped regime can be delayed by adding electrons into the already populated $d_{xz/yz}$ band with a top-gate. In turn, the action of a back-gate is associated with filling an additional high-energy d_{xy} subband, prospectively leading to the formation of a fragile $s_{\pm}$-wave superconducting state.

2. Results

2.1. Double-Gate Field-Effect Device

Whereas back-gate control of the 2-DEG properties is routinely realized in $SrTiO_3$-based interfaces, efficient top-gating has proven to be more challenging and has only been achieved in a limited number of studies. Nevertheless, the electrostatic control of the superconducting T_c and the Rashba spin-orbit coupling has been demonstrated in field-effect devices with a top gate evaporated either directly on the $LaAlO_3$ thin film,[20–25] or isolated by an additional dielectric layer.[3,26,27] More recently, the manipulation of quantum orders at the mesoscopic scales with local top gates was demonstrated in Josephson junctions,[28] SQUIDs,[29] quantum dots,[30] and quantum point contact devices.[31] In this work, a 30 × 10 µm Hall bar was first fabricated in a (001)-oriented $LaAlO_3$(8 u.c)/$SrTiO_3$ heterostructure by the amorphous $LaAlO_3$ template method.[3,32] A metallic top-gate separated by a Si_3N_4 dielectric layer was then deposited on the Hall bar using a standard lithography and lift-off process. Finally, a metallic gate was added on the backside of the $SrTiO_3$ substrate. More information on the fabrication of the device can be found in ref. [3] and in Experimental Section. After the sample was cooled down to 4K, both the top-gate voltage, V_{TG}, and back gate voltage, V_{BG}, were first increased to their maximum positive value, beyond the saturation threshold of the resistance, to ensure that no hysteresis would occur during further gate sweeps.[33] In the following, we will compare the evolution of the 2DEG properties when electrostatically doped with a back-gate or a top-gate voltage. However, since the two dielectric materials have different thicknesses and permittivities ($\varepsilon_r^{SrTiO_3} \simeq 24000$, $\varepsilon_r^{Si_3N_4} \simeq 7.5$), we will plot the relevant quantities as a function of carrier density and not gate voltages.

2.2. Effect of Top-Gating and Back-Gating on the Electronic Mobility

To understand the role of the two gates and check the operation of the device, we first compare the evolution of the electronic mobility with carrier density when either the top-gate or the back-gate voltage is changed. The total carrier density, n_{2D}, is first extracted by combining the Hall effect and gate capacitance measurements at 4 K[2,34] as explained in Experimental Section, from which the mobility $\mu = 1/e\, n_{2D} R_s$ is deduced (R_s is the sheet resistance). Note that the electronic mobility considered here is the weighted sum of the mobilities in each subband. The results are summarized in **Figure 2**c. In both cases, μ increases monotonically with n_{2D} in the entire gating range, but the slope is much sharper for V_{BG} than for V_{TG}. Such behavior is consistent with previous results reported in the literature on conventional semiconducting hetero-interfaces.[35] It can be qualitatively understood by considering the sketches presented in Figure 2a,b,

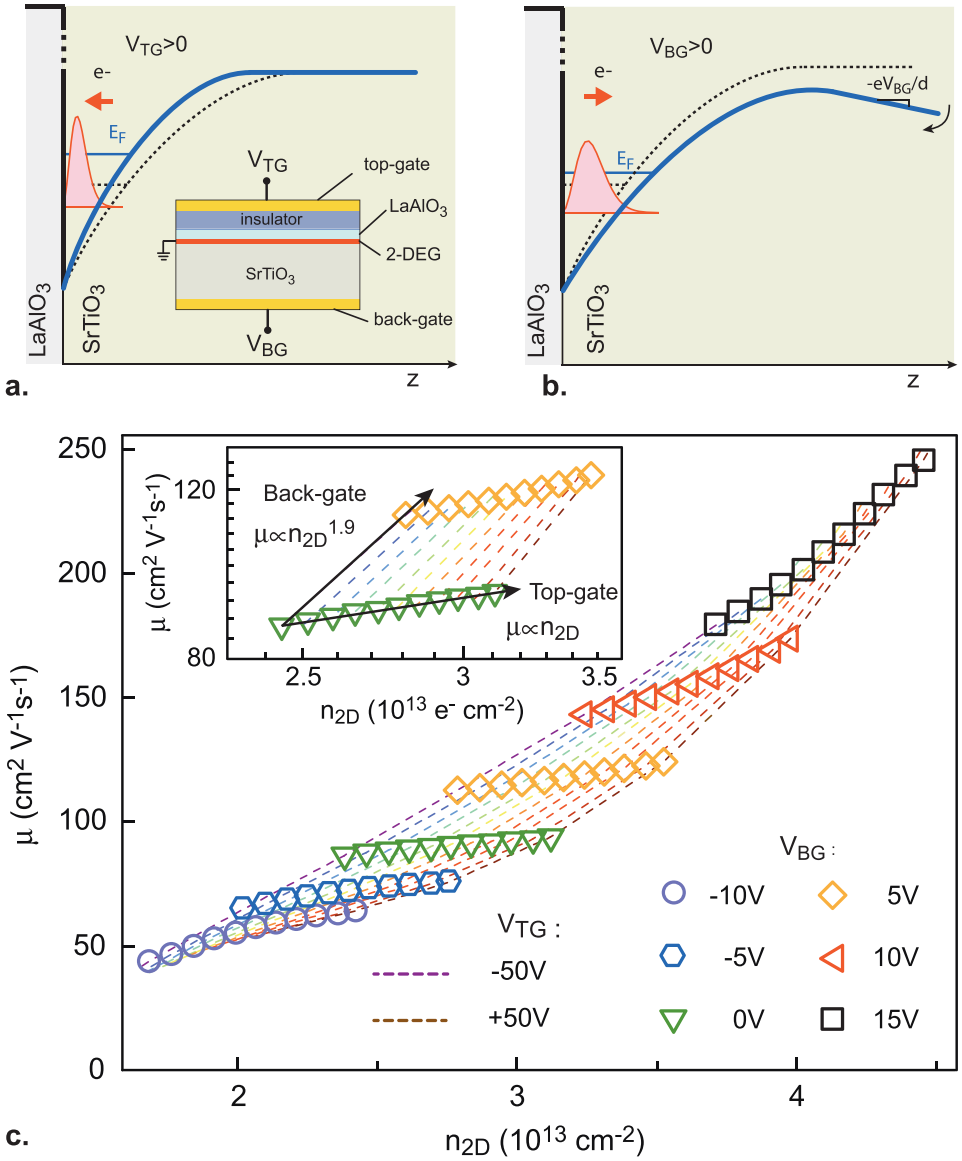

Figure 2. a,b) Illustration of the difference between top-gating (a) and back-gating (b) on the extension of the 2-DEG. In both panels, the black dotted line (blue full line) represents the conduction band profile before (after) applying the gate voltage. While a positive top gate voltage marginally affects the potential well and results in a further spatial confinement of the electronic wave packet (in red), a positive back-gate voltage causes a significantly larger band bending and tends to further delocalize electrons in $SrTiO_3$. In both cases, the Fermi energy E_F increases when a positive top-gate or back-gate voltage is applied. Inset: general scheme of the field-effect device considered in this study. During the experiment, the 2-DEG is kept at the electrical ground of the set-up. c) Electronic mobility μ, plotted as a function of n_{2D}. Symbols of a given color correspond to the same value of V_{BG}. Values of V_{TG} are represented by dotted lines of different colors from $V_{TG} = -50$V to $V_{TG} = +50$ V in step of 10 V. Inset : zoom on the data at $V_{BG} = 0$ V and $V_{BG} = 5$ V plotted on a logarithmic scale. Empirically, we find $\mu \propto n_{2D}^{\gamma}$ with $\gamma_{BG} \simeq 1.9 > \gamma_{TG} \simeq 1.0$.

which explain the main differences between the two types of electrostatic doping execution. On the one hand, increasing V_{TG} makes the confining potential sharper because of charges accumulation, which tends to attract the electrons toward the interface and limits their extension in $SrTiO_3$ (panel a). On the other hand, doping with V_{BG} repels the electrons from the interface by "pulling down" the conduction band in the $SrTiO_3$ substrate, thus deconfining the 2-DEG deeper in the $SrTiO_3$ substrate which is naturally less disordered than the interface[2,22] (panel b). From a more quantitative perspective, in a 2-DEG with several 2D subbands, the mobility is predicted to scale as a power-law of the density ($\mu \propto n_2D^{\gamma}$).[35] Hirakawa et al. demonstrated theoretically, and confirmed experimentally, that the exponent γ is larger when using a back-gate rather than a top-gate.[36] In line with this, we find that at each point of the phase diagram (V_{BG}, V_{TG}), the variation of μ with n_{2D} can be locally approximated by a power-law (inset Figure 2c). Although the exponents γ_{BG} and γ_{TG} vary in the phase diagram, the hierarchy $\gamma_{BG} > \gamma_{TG}$ is always satisfied in agreement with the prediction.[36] For example, for $V_{BG} = 0$ V we obtain $\gamma_{BG} \simeq 1.9 > \gamma_{TG} \simeq 1$ (inset Figure 2c), which

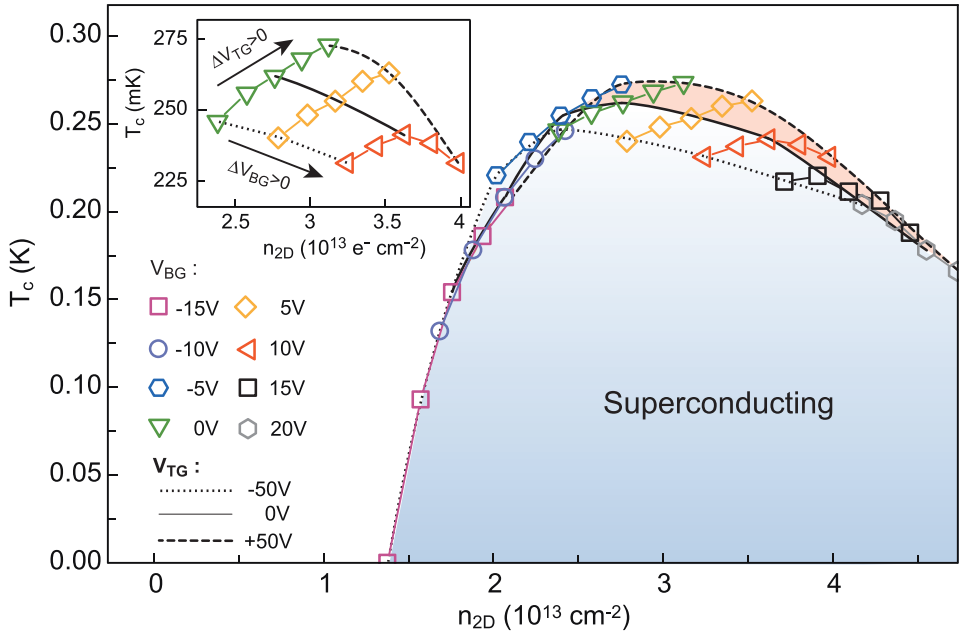

Figure 3. Superconducting critical temperature defined at a 50% drop of the normal resistance plotted as a function of n_{2D}. Inset : magnification of the same data that emphasizes the bifurcation points in the dependence of T_c on n_{2D}. For example at the point (V_{BG} = 0V, V_{TG} = 0V) a positive back-gate voltage step ΔV_{BG} generates a decrease in T_c whereas a positive top-gate voltage step ΔV_{TG} generates an increase in T_c.

corresponds to exponent values comparable with those measured in GaAs/$Al_xGa_{1-x}As$ heterojunctions.[36] In particular, values of γ close to 1 have been associated to Coulomb scattering from ionized donors in the $Al_xGa_{1-x}As$ layer.[35]

2.3. Effect of Top-Gating and Back-Gating on Superconductivity

We now focus on the superconducting properties of our device. All the resistance versus temperature curves measured for the different top-gate and back-gate voltages are shown in the Supporting Information. At low temperature, superconductivity emerges at a critical density, $n_{2D} \simeq 1.4 \times 10^{13}$ .cm^{-2} (**Figure 3**). The T_c then follows a dome-shaped dependence on n_{2D} with a maximum value of $T_c^{max} \simeq 260$ mK, similar to previous observations in $SrTiO_3$-based interfaces.[1] At the lowest and highest carrier densities, T_c displays the same dependence on n_{2D} regardless of the gate being used. However, our data reveal a very peculiar behavior for intermediate values close to the optimal doping: a bifurcation is observed in the T_c dependence on n_{2D} depending on which gate is used. For instance, at V_{BG} = 0 V, adding electrons with a back-gate reduces T_c, whereas adding electrons with a top-gate increases T_c (Figure 3 and inset). The region of higher T_c in red color in the phase diagram of Figure 3 is not accessible resorting solely to a back-gate. Thanks to the two control parameters (V_{TG} and V_{BG}), the two branches of the bifurcation can be followed reversibly.

2.4. Schrödinger–Poisson Numerical Simulations

The presence of a bifurcation in the T_c dependence on n_{2D} shows that in $LaAlO_3/SrTiO_3$ 2-DEG the superconducting T_c is not solely determined by the absolute carrier density but also most likely by the sub-bands occupancy configuration. The key element to understand the bifurcation is the underlying mechanism that leads to the suppression of T_c in the overdoped regime. It has been shown that in disordered two-band superconductors having repulsively coupled condensates (the so-called $s_\pm$-wave superconductors), scattering processes between bands with opposite-sign gaps are pair-breaking and can lead to a suppression of T_c.[37] Trevisan et al. suggested that such mechanism could be responsible for the reduction of T_c in the overdoped regime of (001)-oriented $LaAlO_3/SrTiO_3$ interfaces.[13] The recent observation of single-gap to two-gap superconductivity transition associated to a decrease in T_c in a (110)-oriented $LaAlO_3/SrTiO_3$ interface, consistent with $s_\pm$-wave superconductivity, supports this proposal,[16,17] although this system has some significant differences in the band structure with respect to the conventional (001)-orientation discussed here. Following this approach, we interpret the optimal doping point T_c^{max} in $LaAlO_3/SrTiO_3$ as the filling threshold of a new band, which accommodates a second superconducting gap repulsively coupled to the first one. To support this claim, we examine the band structure in the interfacial quantum well by solving the coupled Schrödinger and Poisson equations self-consistently in the presence of a back-gate (V_{BG}) and a top-gate (V_{TG}) voltage.

The numerical simulations, account for the electric field dependence of the $SrTiO_3$ permittivity, ε_R,[38] and the boundary conditions imposed on the conduction band by the back-gate voltage V_{BG} (see Supporting Information for details). The total carrier densities n_{2D} used in the simulations are extracted from the combination of the Hall effect and gate capacitance measurements as previously discussed and correspond to those used in Figure 2c. **Figure 4**a shows an example

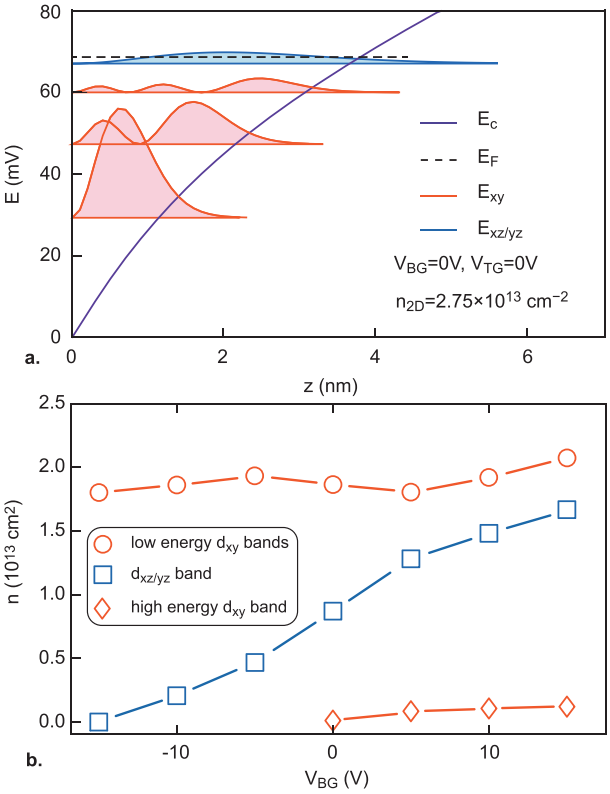

Figure 4. a) Result of the numerical simulation of coupled Schrödinger and Poisson equations showing the spatial dependence of conduction band energy (E_c), the energies (E_{xy}, $E_{xz/yz}$) and the square modulus of the wave functions of the d_{xy} and $d_{xz/yz}$ subbands for [V_{BG} = 0 V, V_{TG} = 0 V] and $n_{2D} = 2.75 \times 10^{13}$ cm^{-2}. The dashed line show the Fermi energy E_F. b) Back-gate voltage dependence of the carrier densities in the lowest d_{xy} subbands, the $d_{xz/yz}$ subband and the high-energy d_{xy} subband extracted from the numerical simulations (V_{TG} = 0 V).

of band structure simulation obtained for a carrier density of $n_{2D} \simeq 2.75 \times 10^{13}$ cm^{-2} corresponding to the optimal doping point $T_c^{max} \simeq 260$ mK. We plot the spatial dependence of the conduction band, the energies, and the square modulus of the wave functions for the different t_{2g} subbands. In this example, three low energy d_{xy} subbands and one high-energy $d_{xz/yz}$ subband are filled. Corresponding carrier densities derived from simulations in the entire back-gating range, are reported on Figure 4b. At the lowest carrier density, V_{BG} = −15 V, only low energy d_{xy} subbands are filled. When the electron density is further increased with the back-gate voltage, the $d_{xz/yz}$ subbands start to be populated, leading to a progressive delocalization of the 2-DEG in the $SrTiO_3$ substrate upon gating. Because the $d_{xz/yz}$ subbands have a higher density of states than the d_{xy} one (by a factor ≃4.4), superconductivity emerges as expected in a BCS picture. The distribution of electrons in the d_{xy} and $d_{xz/yz}$ subbands is consistent with the gate dependence of the Hall effect (Supporting Information). For $V_{BG} \simeq 5$V, a d_{xy} replica sitting higher in energy than the $d_{xz/yz}$ subband is also populated providing a natural ground for two-gap superconductivity.

We now focus in more details on the behavior of superconductivity close to the optimal doping point and look at the results of simulations for a sequence of different back-gate and top-gate voltage steps in this region of the phase diagram (**Figure 5**). Starting with a carrier density of $n_{2D} \simeq 1.5 \times 10^{13}$ cm^{-2} (V_{BG} = −20V, V_{TG} = 0V) in the weakly insulating region, we see that three low-energy d_{xy} subbands are occupied (point A in panel a). The inset illustrates the corresponding point (red circle) in the generic phase diagram of $LaAlO_3/SrTiO_3$ interfaces. When the electron density is further increased with the back-gate voltage, the $d_{xz/yz}$ subbands start to be populated and the T_c rises until it eventually reaches its maximum value (point B in panel 5b). We now consider panels (c) and (d) that show the difference between a top-gate voltage step, ΔV_{TG} = 50 V, and a back-gate voltage step, ΔV_{BG} = 5V, which both produce a similar carrier density variation $\Delta n_{2D} \simeq 4 \times 10^{12}$ cm^{-2} beyond the optimal doping. For $\Delta V_{BG} > 0$, a new d_{xy} subband is populated under the combined effects of the electron density increase and the deconfinement of the quantum well (panel 5c). In contrast to the low-energy d_{xy} subbands that reside at the bottom of the quantum well, this new band extends deeper into the substrate. Because of the coupling with the $d_{xz/yz}$ band, a second superconducting gap is likely to open in this band, prospectively leading to the formation of a $s_{\pm}$-wave superconducting state as proposed by Trevisan et al.[13] and observed in (110)-oriented interfaces.[16,17] We therefore expect T_c to decrease in the overdoped region because of interband scattering (point C). In contrast, for $\Delta V_{TG} > 0$, the confining potential well becomes sharper as suggested in Figure 2a, and the d_{xy} subband is repelled to higher energy (panel 5d). The electron density in the $d_{xz/yz}$ subbands increases, which produces a further increase in T_c in the single-gap superconducting regime (point D). Filling the high-energy d_{xy} subband is delayed, but it eventually occurs with a further increase of the top-gate voltage. The two different electrostatic doping executions (panels 5c and 5d) generate two nonequivalent subbands occupancy configurations that explain the bifurcation in the dependence of T_c (n_{2D}) in the vicinity of optimal doping (Figure 3). Whereas increasing V_{BG} triggers a two-gap $s_{\pm}$-wave superconducting state of reduced T_c, increasing V_{TG} maintains the system in the single gap regime.

3. Discussion

Alternative scenarios, mostly involving multiband effects, can be considered to explain the dome-like shape of T_c as a function of gate voltage. For instance, Gariglio et al. correlate the non-monotonic gate-dependent T_c to a nonmonotonic variation of the 3D carrier density, n_{3D}, at the interface.[39] The effective thickness of the 2-DEG, needed to determine n_{3D}, is inferred from a systematic comparison of the parallel and perpendicular depairing magnetic fields in the superconducting phase diagram. A strong deconfinement of the 2-DEG with back-gate voltage takes place in the overdoped regime leading to a decrease in n_{3D} density while n_{2D} continues to increase. Although we do observe an increase of the 2-DEG spatial extension in our simulations, it does not seem to be sufficient to produce a drop in the n_{3D}, whose gate evolution remains monotonic in our case. Maniv et al. probed the area of the Fermi surface by using the Shubnikov–de Haas (SdH) effect and found that the population of mobile electrons associated

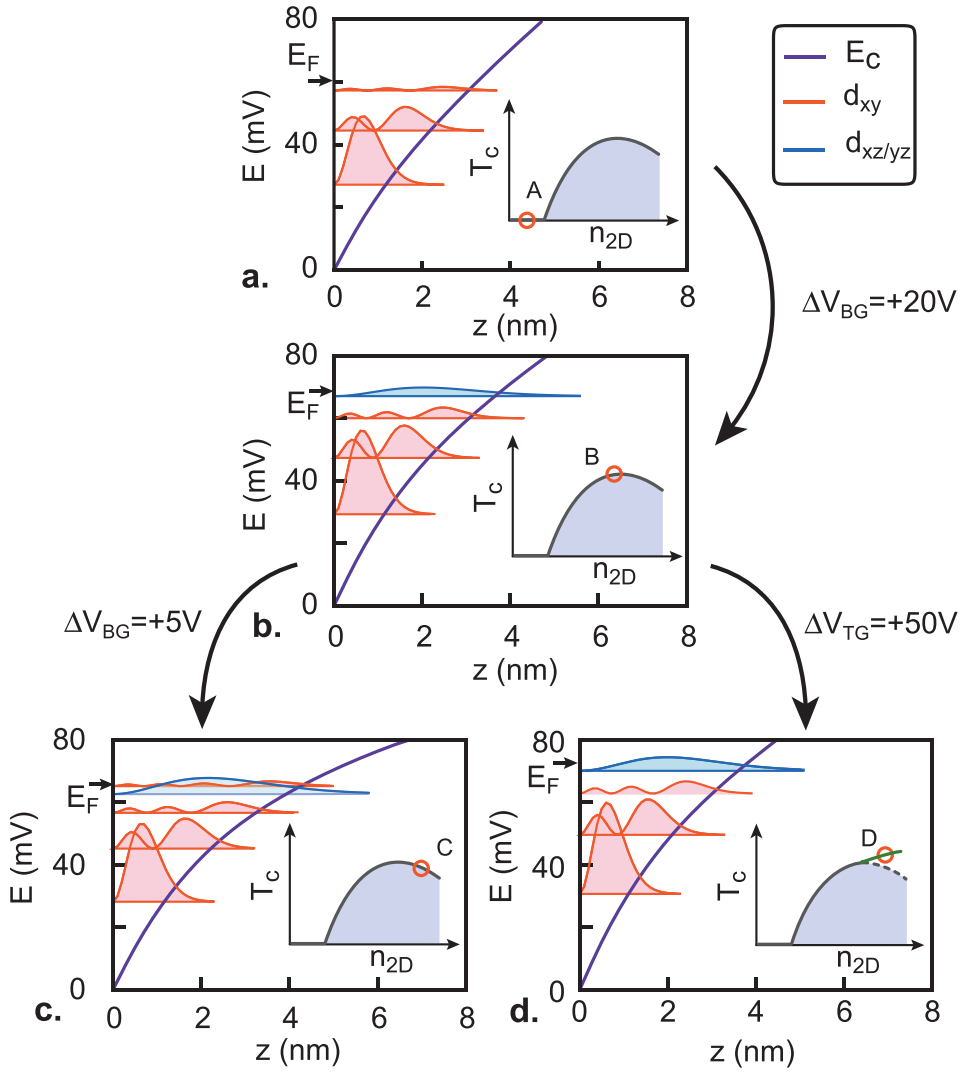

Figure 5. Results of the numerical simulations of coupled Schrödinger and Poisson equations showing the spatial dependence of conduction band energy, (E_c), the energies (E_{xy}, $E_{xz/yz}$) and the square modulus of the wave functions of the d_{xy} and $d_{xz/yz}$ electrons for different carrier densities corresponding to a sequence of back-gate and top-gate voltage steps: a) [$V_{BG} = -20$ V, $V_{TG} = 0$ V] and $n_{2D} = 1.5 \times 10^{13}$ cm^{-2}, b) [$V_{BG} = 0$V, $V_{TG} = 0$V] and $n_{2D} = 2.75 \times 10^{13}$ cm^{-2}, c) [$V_{BG} = +5$V, $V_{TG} = 0$V] and $n_{2D} = 3.16 \times 10^{13}$ cm^{-2}), d) [$V_{BG} = 0$V, $V_{TG} = +50$V] and $n_{2D} = 3.13 \times 10^{13}$ cm^{-2}. The insets schematically indicate the corresponding carrier densities in the superconducting phase diagram (red circles).

with the highest energy occupied band varies nonmonotonically with gate voltage, thus explaining the gate dependence of T_c.[40] They ascribed this peculiar carrier density evolution to repulsive electronic correlations between bands that repels the highest energy band and proposed a model that reproduces well the experimental observations. We could not access the SdH regime in this work due to limited magnetic field and rather low electronic mobilities. While we cannot rule out this alternative scenario, in our case, the analysis of nonlinear Hall effect and capacitance measurements is more consistent with a monotonous increase of both electrons populations. More recently, an extended s-wave symmetry of the gap has been proposed to explain the gate dependence of T_c.[41] Although little is known on the exact symmetry of the superconducting gap, tunneling and microwave conductivity experiments are more in favor of a nodeless isotropic gap.[42–44]

4. Conclusion

In conclusion, we measured the low-temperature transport behavior of a field-effect $LaAlO_3/SrTiO_3$ device, whose electron density can be tuned simultaneously by means of a back-gate and a top-gate. In the superconducting state, we evidenced a bifurcation in the T_c dependence on n_{2D} that we relate to the filling threshold of a high-energy d_{xy} subband using self-consistent Schrödinger–Poisson calculation of the quantum well band structure. Close to the optimal doping point T_c^{max}, a top-gate voltage step produces an increase in T_c whereas a back-gate voltage step generates a decrease in T_c, corresponding respectively, to a single-band and a two-band superconducting state. In the latter case, a repulsive coupling between the two condensates leads to the formation of a $s_{\pm}$-wave superconducting state in which pair-breaking inter-band scattering suppresses superconductivity hence providing a generic

explanation for the dome-shaped phase diagram of T_c. Experiments on $LaAlO_3/SrTiO_3$ Josephson junctions demonstrated the presence of π-shift Josephson channels, which supports the formation of such a two-gap $s_{\pm}$-wave superconducting state in this system.[4,18] Interestingly, such unconventional pairing state has been predicted to be topologically nontrivial.[45]

5. Experimental Section

Sample Growth and Device Fabrication: TiO_2 termination was first achieved on a (001)-oriented $SrTiO_3$ substrate by a buffered HF treatment followed by annealing. The template of a Hall bar with contact pads was then defined by evaporating an amorphous $LaAlO_3$ layer through a resist patterned by optical lithography.[32] After a lift-off process, a thin layer of crystalline $LaAlO_3$ (8 u.c) was grown on the amorphous template by pulse laser deposition at a growth rate of ≈0.2 Å s^{-1} such that only the areas directly in contact with the substrate (Hall bar and contact pads) were crystalline. A KrF excimer (248 nm) laser was used to ablate the single-crystalline $LaAlO_3$ target at 1 Hz, with a fluence between 0.6 and 1.2 J cm^{-2} under an O_2 pressure of 2×10^{-4} mbar. The substrate was typically kept at 650 °C during the growth, monitored in real-time by RHEED. After the growth, the sample was cooled down to 500 °C under a O_2 pressure of 1×10^{-1} mbar. The O_2 pressure was then further increased to 400 mbar to reduce the presence of oxygen vacancies for 30 min before being cooled down to room temperature. The 2-DEG forms at the interface between the crystalline $LaAlO_3$ layer and the $SrTiO_3$ substrate. Such method has already been used to fabricate ungated 500 nm wide channels without noticeable alteration of the 2DEG properties.[32] Once the channel is defined, a 500 nm thick Si_3N_4 dielectric layer was deposited on the Hall bar by a lift-off process. After this step, a gold top-gate layer was deposited and lifted-off to cover the Hall bar. A metallic back gate was also added at the end of the process. A scheme of the device is shown in Supporting Information.

Carrier Density: The Hall effect was measured in a low magnetic field range ($B < 5$T) for different values of the back-gate voltage V_{BG} and top-gate voltage V_{TG} (see Figure S1, Supporting Information). As already reported in $LaAlO_3/SrTiO_3$ 2-DEG, the Hall voltage is linear in magnetic field in the low carrier density regime ($V_G < 0$), and the carrier density is correctly extracted from the slope of the Hall voltage V_H (i.e., $n_{Hall} = IB/eV_H$ where I is the bias current and B the magnetic field). This was no longer the case in the high carrier density regime ($V_G > 0$), where V_H is not linear with B because of multiband transport.[2,34] In this case, n_{Hall} measured in the $B \to 0$ limit did not give the correct carrier density and showed a nonmeaningful decrease with gate voltage. The correct dependence of the total carrier density n_{2D} with V_{BG} can be retrieved from the charging curve of the gate capacitance $C(V_{BG})$:

$$n_{2D}(V_{BG}) = n_S(V_{BG} = -15\text{V}) + \frac{1}{eA}\int_{-15\text{V}}^{V_{BG}} C(V)\mathrm{d}V \quad (1)$$

where A is the area of the capacitor. Figure S2, Supporting Information shows the variation of n_{2D} with top-gate and back-gate voltages extracted from the combination of the Hall effect and gate capacitance measurements.

Supporting Information

Supporting Information is available from the Wiley Online Library or from the author.

Acknowledgements

The authors thank G. Venditti, M. Grilli, and S. Caprara for very fruitful discussions. This work was supported by the French CNRS through a PICS program (S2S) and by the ANR PRC (QUANTOP), by the French RENATECH network (French national nanofabrication platform) and by the DGA. S. The authors acknowledge the funding received from the project Quantox of QuantERA ERA-NET Cofund in Quantum Technologies (Grant Agreement N. 731473) implemented within the European Union's Horizon 2020 Program and from the COST project Nanocohybri-Action CA16218.

Conflict of Interest

The authors declare no conflict of interest.

Data Availability Statement

The data that support the findings of this study are available from the corresponding author upon reasonable request.

Keywords

field-effect device, multiband, oxide interfaces, superconductivity

Received: June 23, 2022
Published online:

[1] A. Caviglia, S. Gariglio, N. Reyren, D. Jaccard, T. Schneider, M. Gabay, S. Thiel, G. Hammerl, J. Mannhart, J.-M. Triscone, *Nature* **2008**, *456*, 624.
[2] J. Biscaras, N. Bergeal, S. Hurand, C. Grossetête, A. Rastogi, R. C. Budhani, D. LeBoeuf, C. Proust, J. Lesueur, *Phys. Rev. Lett.* **2012**, *108*, 247004.
[3] S. Hurand, A. Jouan, C. Feuillet-Palma, G. Singh, J. Biscaras, E. Lesne, N. Reyren, A. Barthélémy, M. Bibes, J. E. Villegas, C. Ulysse, X. Lafosse, M. Pannetier-Lecoeur, S. Caprara, M. Grilli, J. Lesueur, N. Bergeal, *Sci. Rep.* **2015**, *5*, 12751.
[4] D. Stornaiuolo, S. Gariglio, A. Fête, M. Gabay, D. Li, D. Massarotti, J.-M. Triscone, *Phys. Rev. B* **2014**, *90*, 235426.
[5] L. Taillefer, *Annu. Rev. Condens. Matter Phys.* **2010**, *1*, 51.
[6] B. Keimer, S. A. Kivelson, M. R. Norman, S. Uchida, J. Zaanen, *Nature* **2015**, *518*, 179.
[7] Z. S. Popovic, S. Satpathy, R. M. Martin, *Phys. Rev. Lett.* **2008**, *101*, 256801.
[8] P. Delugas, A. Filippetti, V. Fiorentini, D. I. Bilc, D. Fontaine, P. Ghosez, *Phys. Rev. Lett.* **2011**, *106*, 166807.
[9] N. Scopigno, D. Bucheli, S. Caprara, J. Biscaras, N. Bergeal, J. Lesueur, M. Grilli, *Phys. Rev. Lett.* **2016**, *116*, 026804.
[10] M. Salluzzo, J. C. Cezar, N. B. Brookes, V. Bisogni, G. M. De Luca, C. Richter, S. Thiel, J. Mannhart, M. Huijben, A. Brinkman, G. Rijnders, G. Ghiringhelli, *Phys. Rev. Lett.* **2009**, *102*, 166804.
[11] D. Valentinis, S. Gariglio, A. Fête, J.-M. Triscone, C. Berthod, D. van der Marel, *Phys. Rev. B* **2017**, *96*, 094518.
[12] G. Singh, A. Jouan, L. Benfatto, F. Couëdo, P. Kumar, A. Dogra, R. C. Budhani, S. Caprara, M. Grilli, E. Lesne, A. Barthélémy, M. Bibes, C. Feuillet-Palma, J. Lesueur, N. Bergeal, *Nat. Commun.* **2018**, *9*, 407.
[13] T. V. Trevisan, M. Schütt, R. M. Fernandes, *Phys. Rev. Lett.* **2018**, *121*, 127002.
[14] R. M. Fernandes, J. T. Haraldsen, P. Wölfle, A. V. Balatsky, *Phys. Rev. B* **2013**, *87*, 014510.
[15] G. Binnig, A. Baratoff, H. E. Hoenig, J. G. Bednorz, *Phys. Rev. Lett.* **1980**, *45*, 1352.

[16] G. Singh, A. Jouan, G. Herranz, M. Scigaj, F. Sánchez, L. Benfatto, S. Caprara, M. Grilli, G. Saiz, F. Couëdo, C. Feuillet-Palma, J. Lesueur, N. Bergeal, *Nat. Mater.* **2019**, *18*, 948.
[17] G. Singh, G. Venditti, G. Saiz, G. Herranz, F. Sanchez, A. Jouan, C. Feuillet-Palma, J. Lesueur, M. Grilli, S. Caprara, N. Bergeal, *Phys. Rev. B* **2022**, *105*, 064512.
[18] G. Singh, C. Guarcello, E. Lesne, D. Winkler, T. Claeson, T. Bauch, F. Lombardi, A. D. Caviglia, R. Citro, Ma. Cuoco, A. Kalaboukhov, *npj Quantum Mater.* **2022**, *7*, 2.
[19] D. Stornaiuolo, D. Massarotti, R. Di Capua, P. Lucignano, G. P. Pepe, M. Salluzzo, F. Tafuri, *Phys. Rev. B* **2017**, *95*, 40502.
[20] M. Hosoda, Y. Hikita, H. Y. Hwang, C. Bell, *Appl. Phys. Lett.* **2013**, *103*, 103507.
[21] P. D. Eerkes, W. G. van der Wiel, H. Hilgenkamp, *Appl. Phys. Lett.* **2013**, *103*, 201603.
[22] W. Liu, S. Gariglio, A. Fête, D. Li, M. Boselli, D. Stornaiuolo, J.-M. Triscone, *APL Mater.* **2015**, *3*, 062805.
[23] S. Goswami, E. Mulazimoglu, L. M. K. Vandersypen, A. D. Caviglia, *Nano Lett.* **2015**, *15*, 2627.
[24] B. Forg, C. Richter, J. Mannhart, *Appl. Phys. Lett.* **2012**, *100*, 053506.
[25] Z. Chen, A. G. Swartz, H.Yoon, H. Inoue, T. A. Merz, D. Lu, Y. Xie, H. Yuan, Y. Hikita, S. Raghu, H. Y. Hwang, *Nat. Commun.* **2018**, *9*, 4008.
[26] S. Hurand, A. Jouan, C. Feuillet-Palma, G. Singh, E. Lesne, N. Reyren, A. Barthélémy, M. Bibes, J. E. Villegas, C. Ulysse, M. Pannetier-Lecoeur M. Malnou J. Lesueur, N. Bergeal, *Appl. Phys. Lett.* **2016**, *108*, 052602.
[27] V. V. Bal, M. M. Mehta, S. Ryu, H. Lee, C. M. Folkman, C. B. Eom, V. Chandrasekhar, *Appl. Phys. Lett.* **2015**, *106*, 212601.
[28] H. Thierschmann, E. Mulazimoglu, N. Manca, S. Goswami, T. M. Klapwijk, A. D. Caviglia, *Nat. Commun.* **2018**, *9*, 2276.
[29] S. Goswami, E. Mulazimoglu, A. M. R. V. L. Monteiro, R. Wölbing, D. Koelle, R. Kleiner, Y. M. Blanter, L. M. K. Vandersypen, A. D. Caviglia, *Nat. Nanotechnol* **2016**, *11*, 861.
[30] G. E. D. K. Prawiroatmodjo, M. Leijnse, F. Trier, Y. Chen, D. V. Christensen, M. von Soosten, N. Pryds, T. S. Jespersen, *Nat. Commun.* **2017**, *8*, 395.
[31] A. Jouan, G. Singh, E. Lesne, D. C. Vaz, M. Bibes, A. Barthélémy, C. Ulysse, D. Stornaiuolo, M. Salluzzo, S. Hurand, J. Lesueur, C. Feuillet-Palma, N. Bergeal, *Nat. Electron.* **2020**, *3*, 201.
[32] D. Stornaiuolo, S. Gariglio, N. J. G. Couto, A. Fête, A. D. Caviglia, G. Seyfarth, D. Jaccard, A. F. Morpurgo, J.-M. Triscone, *Appl. Phys. Lett.* **2012**, *101*, 222601.
[33] J. Biscaras, S. Hurand, C. Feuillet-Palma, A. Rastogi, R. C. Budhani, N. Reyren, E. Lesne, J. Lesueur, N. Bergeal, *Sci. Rep.* **2014**, *4*, 6788.
[34] G. Singh, A. Jouan, S. Hurand, F. Feuillet-Palma, P. Kumar, A. Dogra, R. C. Budhani, J. Lesueur, N. Bergeal, *Phys. Rev. B* **2017**, *96*, 024509.
[35] T. Ando, *J. Phys. Soc. Jpn.* **1982**, *51*, 3900.
[36] K. Hirakawa, H. Sakaki, J. Yoshino, *Phys. Rev. Lett.* **1985**, *54*, 1279.
[37] V. G. Kogan, R. Prozorov, *Phys. Rev. B* **2016**, *93*, 224515.
[38] R. C. Neville, B. Hoeneisen, C. A. Mead, *J. Appl. Phys.* **1972**, *43*, 2124.
[39] S. Gariglio, M. Gabay, J.-M. Triscone, *APL Mater.* **2016**, *4*, 060701.
[40] E. Maniv, M. Ben Shalom, A. Ron, M. Mograbi, A. Palevski, M. Goldstein, Y. Dagan, *Nat. Commun.* **2015**, *6*, 8239.
[41] M. Zegrodnik, P. Wójcik, *Phys. Rev. B* **2020**, *102*, 085420.
[42] C. Richter, H. Boschker, W. Dietsche, E. Fillis-Tsirakis, R. Jany, F. Loder, L. F. Kourkoutis, D. A. Muller, J. R. Kirtley, C. W. Schneider, J. Mannhart, *Nature* **2013**, *502*, 528.
[43] J. A. Bert, K. C. Nowack, B. Kalisky, H. Noad, J. R. Kirtley, C. Bell, H. K. Sato, M. Hosoda, Y. Hikita, H. Y. Hwang, K. A. Moler, *Phys. Rev. B* **2012**, *86*, 060503.
[44] M. Thiemann, M. H. Beutel, M. Dressel, N. R. Lee-Hone, D. M. Broun, E. Fillis-Tsirakis, H. Boschker, J. Mannhart, M. Scheffler, *Phys. Rev. Lett.* **2018**, *120*, 237002.
[45] M. Scheurer, J. Schmalian, *Nat. Commun.* **2015**, *6*, 6005.